THE JOURNAL OF PHYSICAL CHEMISTRY C

Article

pubs.acs.org/JPCC

Dehydrogenation Improvement of $LiAlH_4$ Catalyzed by Fe_2O_3 and Co_2O_3 Nanoparticles

Ziliang Li,[†] Ping Li,[†,*] Qi Wan,[†] Fuqiang Zhai,[‡] Zhiwei Liu,[†] Kuifei Zhao,[†] Ling Wang,[†] Shaoyuan Lü,[†] Liang Zou,[†] Xuanhui Qu,[†,§] and Alex A. Volinsky[||]

[†]Institute for Advanced Materials and Technology, University of Science and Technology Beijing, Beijing 100083, China

[‡]Departament Física Aplicada, EETAC, Universitat Politècnica de Catalunya- BarcelonaTech, 08860 Castelldefels, Spain

[§]State Key Laboratory for Advanced Metals and Materials, University of Science and Technology Beijing, Beijing 100083, China

[||]Department of Mechanical Engineering, University of South Florida, Tampa, Florida 33620, United States

Supporting Information

ABSTRACT: The catalytic effect of two nanoscale transition metal oxides, Fe_2O_3 and Co_2O_3, as additives on the dehydrogenation properties of $LiAlH_4$ after milling are investigated. The onset dehydrogenation temperature for the 5 mol % Fe_2O_3-doped and 5 mol % Co_2O_3-doped samples are 85 and 79 °C lower for the first-stage and 60 and 45 °C lower for the second-stage, respectively, compared with the as-received $LiAlH_4$. The isothermal dehydriding kinetics reveals that the 5 mol % Fe_2O_3-doped sample can release about 7.1 wt % hydrogen in 70 min at 120 °C, whereas as-received $LiAlH_4$ only releases 0.3 wt % hydrogen under the same conditions. From differential scanning calorimetry (DSC) and Kissinger desorption kinetics analyses, the apparent activation energies (E_a) of the 5 mol % Fe_2O_3-doped sample are 54.2 and 86.4 kJ/mol for the first two dehydrogenation stages, resulting in decreases of 42.8 and 50% compared with those of as-received $LiAlH_4$, respectively, which are considerably lowered compared with $LiAlH_4$ doped with other reported catalysts calculated by Kissinger method. X-ray diffraction (XRD), X-ray photoelectron spectroscopy (XPS), and Fourier transform infrared (FTIR) analyses demonstrate that these finely dispersed $Li_2Fe_{2.4}O_{4.6}$, $Fe_{0.957}O$, and various Co oxides contribute to kinetics improvement by serving as active sites for nucleation and growth of dehydrogenated products.

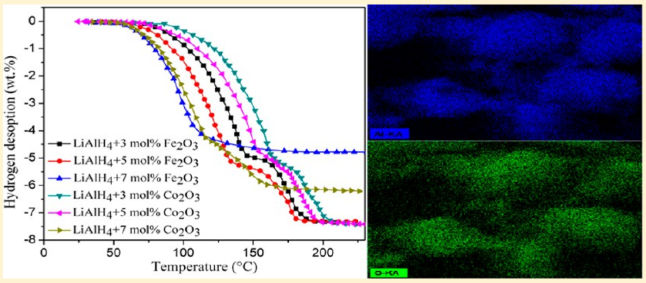

1. INTRODUCTION

The environment and energy crisis drives humanity to find new energy carriers for mobile and stationary applications. As one of the ideal energy carrier candidates for various applications, hydrogen attracts more and more attention due to its environmental friendliness, cost effectiveness and fuel efficiency. However, until now the major obstacle to realizing a hydrogen-based economy is how efficient and safe hydrogen can be stored and released for utilization.[1−3] According to the 2015 hydrogen energy strategy, released by the US Department of Energy, in a viable hydrogen storage system, the practical hydrogen storage material should reach more than 5.5 wt % absorption capacity and have fast desorption rate of 1.5 wt % min^{-1}.[4] Compared with traditional hydrogen storage methods, such as high pressurized gas and cryogenic liquid hydrogen, solid-state hydrogen storage is a promising option, not only because of its high volumetric hydrogen capacity, but also favorable safety considerations.[5−7]

Among various solid-state hydrogen storage materials, lithium aluminum hydride ($LiAlH_4$) is viewed as a potential hydrogen storage material due to its relatively large theoretical hydrogen storage capacity. $LiAlH_4$ has been regarded as a promising candidate both for fundamental research of the absorption/desorption mechanisms and for technological applications.[8] Theoretically, $LiAlH_4$ can desorb 10.5 wt % hydrogen upon heating, according to the following reactions[9]

$$3LiAlH_4 \rightarrow Li_3AlH_6 + 2Al + 3H_2 \quad (T = 150 - 175°C, 5.3\ \text{wt\%H}) \tag{R1}$$

$$Li_3AlH_6 \rightarrow 3LiH + Al + \frac{3}{2}H_2 \quad (T = 180 - 220°C, 2.6\ \text{wt\%H}) \tag{R2}$$

$$3LiH + 3Al \rightarrow 3LiAl + \frac{3}{2}H_2 \quad (T = 400 - 420°C, 2.6\ \text{wt\%H}) \tag{R3}$$

The whole process of R3 only releases 2.6 wt % H_2 and requires heating above 400 °C, which is not considered viable for practical applications. Therefore, it is reasonable to consider the dehydrogenation properties of $LiAlH_4$ during the first two reaction steps for practical applications.

Received: June 13, 2013
Revised: August 7, 2013
Published: August 13, 2013

ACS Publications dx.doi.org/10.1021/jp405844z | J. Phys. Chem. C 2013, 117, 18343−18352

Unfortunately, the high-thermodynamic stability and slow desorption kinetics of $LiAlH_4$ have severely constrained its practical application as a suitable hydrogen storage medium. In order to overcome these obstacles, extensive studies of catalysts incorporated by ball-milling to ameliorate dehydrogenation properties of $LiAlH_4$ have been conducted recently.[10] Up to now, the investigated catalysts fall into the following six categories: (1) pure metals, such as V,[11] Ni,[11−13] Fe,[11,14−16] Ti,[16−20] Sc,[16] and Al;[14] (2) alloys, such as Ti_3Al, $TiAl_3$, Al_3Fe, and $Al_{22}Fe_3Ti_8$;[14,16] (3) carbon-containing materials, such as carbon black,[11] CNFs,[21] and TiC;[22] (4) halides, such as $AlCl_3$,[11] $FeCl_3$,[11] $TiCl_3•1/3AlCl_3$,[17,23] VBr_3,[24] $HfCl_4$,[25] $ZrCl_4$,[25] $LaCl_3$,[26] VCl_3,[21] $TiCl_3$,[27] $ZnCl_2$,[27] $NiCl_2$,[28] TiF_3,[29] NbF_5,[30] $MnCl_2$,[31] K_2TiF_6,[32] $TiCl_4$,[33] and NH_4Cl;[34] (5) metallic oxides, such as TiO_2,[35] Nb_2O_5,[36] Cr_2O_3,[36] and $MnFe_2O_4$;[37] and (6) the others such as nanosized TiH_2,[38] $Ce(SO_4)_2$,[39] metallic single wall carbon nanotubes,[40] and TiN.[1] Among these catalysts, multivalent transition metal oxides have shown significant catalytic effect on improving the dehydrogenation properties of $LiAlH_4$.[35−37] Meanwhile, reducing the size of catalytic additives to nanoscale is another approach, which can also improve kinetic and thermodynamic properties of hydrogen storage materials.[2,3,12,13,22,35−37] Therefore, nanosized transition metal oxide catalysts exhibit huge potential for improving the hydrogen storage properties of $LiAlH_4$.

To our knowledge, no studies have been reported on $LiAlH_4$ doped with Fe_2O_3 and Co_2O_3. According to Zhang et al.,[41] mesoporous Fe_2O_3 exhibits a prominent effect on improving the dehydrogenation properties of $LiBH_4$. Recently, it has also been reported that Fe^{3+} and Fe could provide favorable effect on enhancing the dehydrogenation properties of $LiAlH_4$.[14−16,37] Thus, Fe_2O_3 could be selected as catalyst precursor to investigate its effect on the dehydrogenation properties of $LiAlH_4$. Meanwhile, previous investigations showed that the Co oxide additives improve the dehydrogenation kinetics of MgH_2[42] and $LiBH_4/2LiNH_2/MgH_2$ system.[43] Therefore, it is reasonable to assume that Fe_2O_3 and Co_2O_3 can significantly improve the hydrogen storage properties of $LiAlH_4$.

In the present work, the effects of Fe_2O_3 and Co_2O_3 additives on the dehydrogenation properties of $LiAlH_4$ were investigated by utilizing a pressure−composition−temperature (PCT) apparatus, thermogravimetry (TG), and differential scanning calorimetry (DSC). The catalytic mechanism was demonstrated by analyzing the results of Fourier transform infrared spectroscopy (FTIR), scanning electron microscopy (SEM), X-ray diffraction (XRD), and X-ray photoelectron spectroscopy (XPS).

2. EXPERIMENTAL SECTION

2.1. Sample Preparation. $LiAlH_4$ (≥95% pure), the high-purity nano-oxides of Fe_2O_3 (30 nm, spherical, 99.5%), and Co_2O_3 (>99%, ∼90 nm) were purchased from Sigma Aldrich Co., and all materials were used as received without any further purification. All operations were carried out in the high-purity argon-filled glovebox (H_2O, <10 ppm; O_2, <10 ppm). About 1.5 g of $LiAlH_4$ was mixed with various mole fractions of Fe_2O_3 and Co_2O_3 nanopowders and then the mixture was loaded into a stainless milling vial with a ball to powder weight ratio of 20:1. Subsequently, the samples were ball-milled for 30 min by using a high-energy Spex mill (QM-3B) at the rate of 1200 rpm. After every 10 min of milling, the samples were cooled for 5 min.

2.2. Characterization. Hydriding/dehydriding properties of as-received and doped $LiAlH_4$ samples were measured by a Sieverts-type PCT apparatus (Beijing Nonferrous Metal Research Institute, China). This apparatus can be operated up to 10 MPa and at 600 °C. It mainly consist of a pressure transducer and a reactor. The former was used to connect with the pressure transducer and thermocouple, and the reactor consisted of two parts, the heater and the sample vessel. From the magnitude of the hydrogen pressure change, we could calculate the amount of the hydrogen absorbed and desorbed.[22,44] About 0.3 g of sample was loaded into the vessel. For dehydrogenation (the first two steps), the sample was heated to 250 °C at a heating rate of 5 K min^{-1} under 0.1 atm pressure. The dehydrogenation amounts, calculated for all the samples, were converted to pure $LiAlH_4$ with the elimination of various impurities.

The synchronous DSC/TG analysis was conducted by using a NETZSCH STA 449C under high-purity (99.99%) Ar flow 50 mL min^{-1}. Typically, the sample mass was 5 mg. Heating runs were performed at different rates (6, 9, and 12 K min^{-1}) from 35 to 300 °C, respectively. Then the dehydriding kinetics of the doped $LiAlH_4$ samples was calculated by using DSC results according to the Kissinger method.

The microstructure of as-received and doped samples was observed by using the SEM (ZEISS EVO 18, Germany). Sample preparation for the SEM measurement was carried out inside the glovebox, and then the samples were transferred to the SEM chamber. The elemental mapping was used to study the distribution of catalyst.

FTIR analysis of the pure and doped samples after ball-milling was carried out by using a Bruker Vector 22 FTIR spectrometer. The FTIR spectra were recorded from 750 to 2000 cm^{-1} with a spectral resolution of 4 cm^{-1}.

The phase structures of milled samples, before and after desorption, were detected by X-ray diffraction MXP21VAHF X-ray diffractometer (XRD with Cu Ka radiation, 40 kV, 200 mA) at room temperature. The X-ray intensity was tested over the 2θ angle ranged from 10 to 80° with a scanning velocity of 0.02° per step. Before measurements, the samples were coated with parafilm to prevent oxidation during XRD measurements. XPS experiments were performed in an ultrahigh vacuum (UHV) chamber with the base pressure of 3×10^{-13} MPa, equipped with a Perkin-Elmer PHI-5300 XPS spectrometer.

3. RESULTS AND DISCUSSION

3.1. Dehydrogenation Properties Analysis. Figure 1a shows the nonisothermal dehydrogenation properties of as-received $LiAlH_4$, as-milled $LiAlH_4$, and $LiAlH_4$ doped with 5 mol % Fe_2O_3 and Co_2O_3 nanoparticles, respectively. All samples exhibit similar decomposition processes, which include two dehydrogenation steps, corresponding to the first reaction (R1) and the second reaction (R2). By comparing the dehydriding properties of $LiAlH_4$ with and without the dopant, it is clear that doping with the nano-oxide exhibits a quite striking catalytic effect on the dehydriding properties of $LiAlH_4$, not only for the dehydrogenation characteristics of (R1) but also for the second step (R2). For as-received $LiAlH_4$, it starts to release hydrogen at around 155 °C and desorbs about 5.0 wt % hydrogen for the first dehydrogenation step. For the second stage, it starts to dehydrogenate at 200 °C, and about 2.5 wt % hydrogen is released. Thus, a total hydrogen release capacity of 7.5 wt % is obtained below 250 °C. For the as-milled $LiAlH_4$, the onset desorption temperatures for the first two dehydrogenation steps both decreased by about 21 °C, compared with the as-received $LiAlH_4$, attributed to the decrease of the grain size of $LiAlH_4$ by mechanical milling.[32] As seen in Figure 1, the desorption

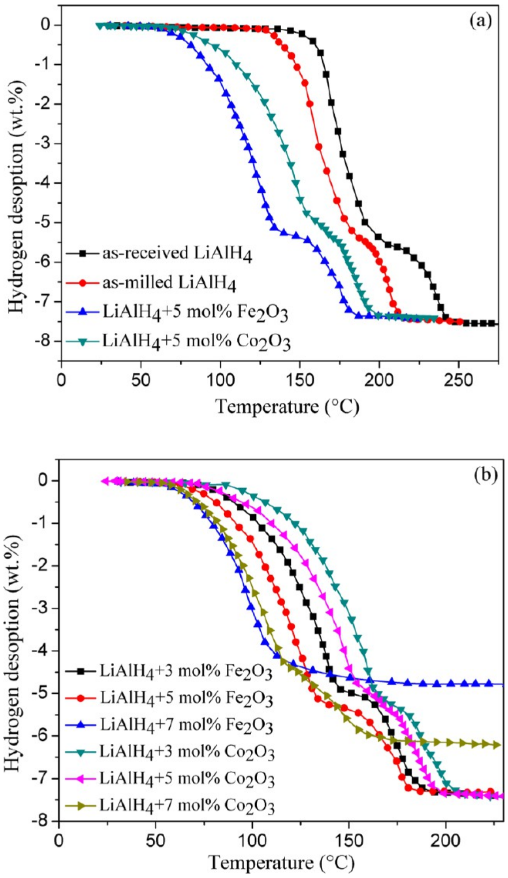

Figure 1. (a) Comparison of thermal desorption profiles of as-received $LiAlH_4$, as-milled $LiAlH_4$, $LiAlH_4$ doped with 5 mol % Fe_2O_3, and Co_2O_3 nanoparticles. (b) $LiAlH_4$ doped with 3, 5, and 7 mol % Fe_2O_3 and Co_2O_3 nanoparticles.

temperature of $LiAlH_4$ decreased significantly by doping Fe_2O_3 and Co_2O_3 nanoparticles, and the Fe_2O_3 nanopowders exhibit more superior catalytic effect than nanosized Co_2O_3. For the 5 mol % Fe_2O_3-doped and 5 mol % Co_2O_3-doped samples, the dehydrogenation process starts at 70 and 76 °C for the first stage, which are 85 and 79 °C lower than that of pristine $LiAlH_4$, respectively. With further heating of the samples, the second-stage occurs at 140 and 155 °C, resulting in a drastic reduction of the desorption temperature onset of $LiAlH_4$ by 60 and 45 °C, respectively. During the first two dehydrogenation processes, 7.4 and 7.3 wt % of hydrogen can be desorbed for the 5 mol % Fe_2O_3-doped and 5 mol % Co_2O_3-doped samples, respectively, which are both close to the theoretical hydrogen release content of pristine $LiAlH_4$. By analyzing the above results, it is concluded that the Fe_2O_3- and Co_2O_3-doped samples exhibit superior catalytic properties by reducing the dehydrogenation temperature onset and improving the desorption kinetics of $LiAlH_4$. Moreover, the dehydrogenation temperatures of 5 mol % Fe_2O_3 doped sample are significantly lower than those of $LiAlH_4$ with various catalysts reported in the literature.[1,36,45]

Figure 1b exhibits the nonisothermal dehydrogenation properties of as-received $LiAlH_4$, as-milled $LiAlH_4$, and $LiAlH_4$ doped with various mole fractions of oxide nanoparticles. All the Fe_2O_3- and Co_2O_3-doped samples start to decompose below 100 °C in the first-stage, as shown in Figure 1b. The 7 mol % Fe_2O_3-doped sample begins to decompose at 58 °C, which is 97 °C lower than that of pure Li Alanate. However, for the samples doped with 3, 5, and 7 mol % Co_2O_3 nanoparticles the initial dehydrogenation temperature lowers to 95, 76, and 62 °C, respectively, slightly higher than the corresponding temperature decrease caused by Fe_2O_3 nanoparticles. In addition, the total hydrogen release of 3−5 mol % oxide-doped samples changes from 7.4 to 7.5 wt %, which is lower than that of the as-received $LiAlH_4$. However, further increase of the additive amount to 7 mol % results in Fe_2O_3-doped and Co_2O_3-doped samples desorption hydrogen content of only 4.8 and 6.2 wt % in the first two dehydrogenation steps, accounting for 63.5 and 82.3% for the total hydrogen release of pure $LiAlH_4$. This phenomenon can be attributed to the fairly low dehydrogenation temperature caused by the excessive catalytic effect leading to a substantial amount of hydrogen released along with the ball-milling process.[30−32,35,37] Compared with other mole fractions of metal oxide additives, it is reasonable to conclude that 5 mol % addition exhibits the optimal dehydrogenation performance, including not only the onset dehydrogenation temperature but also the released hydrogen capacity. As a result, both 5 mol % doped samples are appropriate for analyzing the catalytic effects and mechanisms in the following tests.

In order to further verify the catalytic effects of Fe_2O_3 and Co_2O_3 nanoparticles on the thermal decomposition performance of $LiAlH_4$, DSC/TG measurements have been performed on the samples of as-received $LiAlH_4$, $LiAlH_4$ + 5 mol % Fe_2O_3, and $LiAlH_4$ + 5 mol % Co_2O_3 within the temperature range of 35−300 °C at the heating rate of 6 K min^{-1}, respectively, as shown in Figure 2. For as-received $LiAlH_4$, 7.5 wt % H_2 was released during the first two stages, as shown in Figure 2a, which is in good agreement with the results tested by PCT. Analyzing the DSC curve of the as-received $LiAlH_4$ shows that there are four characteristic peaks in the first two dehydrogenation stages, including two exothermic peaks and two endothermic peaks. The first exothermic peak appears at 154.9 °C, corresponding to the interaction of $LiAlH_4$ with surface hydroxyl impurities, and the first endothermic peak that emerges at 166.4 °C corresponding to $LiAlH_4$ melting.[46] For elevated temperature, the second exothermic peak appears at 184.5 °C, corresponding to the decomposition of liquid $LiAlH_4$ (R1), and the second endothermic peak at 240.0 °C, corresponding to the decomposition of Li_3AlH_6 (R2).[23] As can be seen in Figure 2b,c, both DSC curves only exhibit two characteristic peaks, including one exothermic peak and one endothermic peak, which correspond to the first two dehydrogenation processes. For the $LiAlH_4$ + 5 mol % Fe_2O_3 sample, the thermal event for the doped sample initiates at 83.0 °C, and the exothermic and endothermic peaks appear at 130.3 and 219.0 °C, respectively. Compared with Fe_2O_3 doped sample, the DSC curve of Co_2O_3 doped sample shows that an exothermic reaction occurs between 92.1 and 153.5 °C with an exothermic peak at 136.1 °C, and then between 198.2 and 226.5 °C the endothermic reaction begins with an endothermic peak at 223.0 °C. By analyzing the above DSC results, it is found that the first endothermic peak for doped samples corresponds to the decomposition of solid-state $LiAlH_4$ due to the oxide-doped $LiAlH_4$ starting to decompose prior to melting. Meanwhile, from the TG results in Figure 2b,c it is clear that the two thermal processes in DSC curves correspond exactly to the first two decomposition stages of $LiAlH_4$. The hydrogen release content for 5 mol % Fe_2O_3- and Co_2O_3-doped samples reaches 7.4 and 7.4 wt %, respectively, which is in good agreement with the results measured by PCT (Figure 1). By comparing the dehydrogenation performance of $LiAlH_4$ with and without catalyst measured by DSC and PCT, the onset dehydrogenation temperature tested by DSC is quite higher

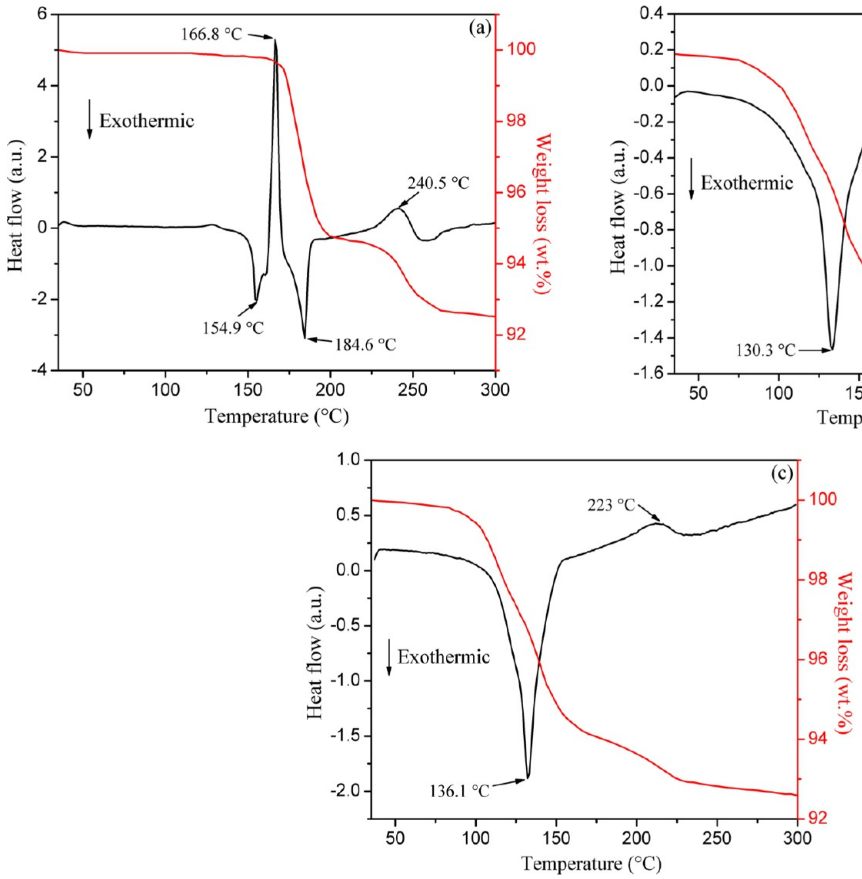

Figure 2. DSC/TG profiles of (a) as-received $LiAlH_4$, (b) $LiAlH_4$ + 5 mol % Fe_2O_3, and (c) $LiAlH_4$ + 5 mol % Co_2O_3 within the 35−300 °C temperature range at a heating rate of 6 °C min^{-1}.

than that tested by PCT (Figure 1). A similar phenomenon also appears in the previous reports of various catalysts,[30,32,35,37] attributed to the different decomposition atmosphere during DSC (1 atm argon) and PCT (0.1 atm H_2) tests, leading to the different driving force for the desorption process.[37]

In order to further illustrate the significant influence of nano-oxide additives on the desorption kinetics of $LiAlH_4$, Figure 3 shows the isothermal dehydrogenation behavior of as-received $LiAlH_4$ at 120 °C and $LiAlH_4$ doped with 5 mol % nano-oxide additives at 90, 120, and 150 °C, respectively. For the as-received $LiAlH_4$, the desorption rate is sluggish at 120 °C, and only 0.7 wt % of hydrogen can be detected within 180 min, demonstrating the perishing desorption kinetics of pristine $LiAlH_4$. However, the 5 mol % Co_2O_3- and Fe_2O_3-doped samples release 4.0 and 4.4 wt % H_2 in 180 min at 90 °C, respectively, indicating that the first dehydrogenation step of $LiAlH_4$ almost completed for the $LiAlH_4$/Fe_2O_3 composites. When heated at 120 °C, about 5.2 and 7.2 wt % hydrogen is released in 120 min for the Co_2O_3-doped and Fe_2O_3-doped samples, illustrating that the second dehydrogenation stage of $LiAlH_4$ has occurred. Further increase in temperature up to 150 °C for only 15−20 min is required to complete the first dehydrogenation step for those two oxide-doped samples, and the dehydrogenation amount reaches 7.2 and 7.4 wt % in 120 min, respectively. Moreover, the Fe_2O_3-doped sample could finish the first dehydrogenation step and desorb about 5.0 wt % of hydrogen in 15 min at 150 °C, indicating significantly improved dehydrogenation kinetics. As a result, the oxide-doped samples exhibit dramatic improvement in the dehydrogenation properties, compared with the as-received $LiAlH_4$.

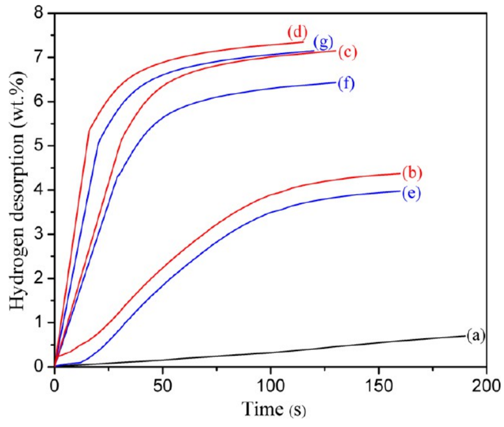

Figure 3. Isothermal dehydrogenation kinetics of (a) as-received $LiAlH_4$ at 120 °C, (b−d) $LiAlH_4$ + 5 mol % Fe_2O_3 at 90, 120, and 150 °C, (e−g) $LiAlH_4$ + 5 mol % Co_2O_3 at 90, 120, and 150 °C, respectively.

3.2. Dehydrogenation Mechanism.

To observe the changes of particle size and morphology of as-received $LiAlH_4$ and the doped samples before and after ball-milling, Figures 4−6 shows the representative SEM micrographs of as-received $LiAlH_4$, as-milled $LiAlH_4$, and $LiAlH_4$ doped with 5 mol % Fe_2O_3 and Co_2O_3 nanopowders, respectively. As seen in Figure 4a, the as-received $LiAlH_4$ sample consists of large irregular polyhedron particles, up to 40 μm in size. However, the shape of as-milled $LiAlH_4$ changes into regular globular particles and their

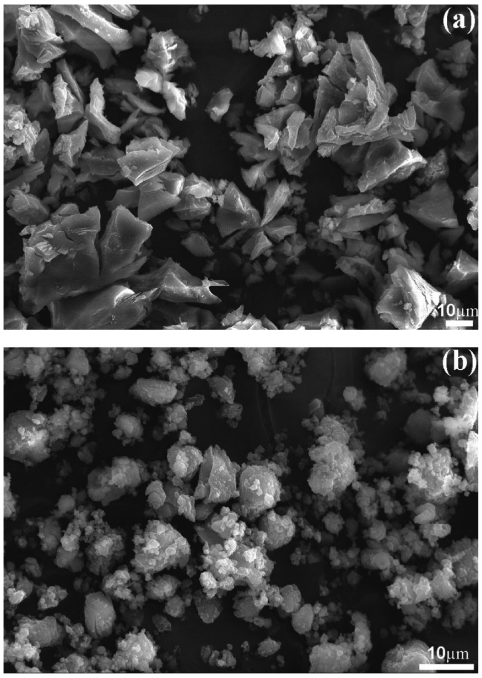

Figure 4. SEM images of (a) as-received $LiAlH_4$ and (b) pure $LiAlH_4$ after 30 min ball-milling.

particle size varies between 3 and 10 μm, as seen in Figure 4b, indicating a significant decrease in the particle size of $LiAlH_4$ after ball-milling. Figures 5a and Figure 6a exhibit the microstructure of $LiAlH_4$ doped with 5 mol % Fe_2O_3 and Co_2O_3 after mechanical ball-milling for 30 min. Microscopically, the doped samples after milling have disordered surface, and the initial particles break into smaller particles with the size of ∼6 μm. The collision and friction during ball-milling make the sizes decrease and cracked surfaces occur. The distributions of all the species in the mixture are uniform, which can be seen from the elemental maps of Al, O, Fe (Co), as shown in Figures 5 and 6. This means that the oxide catalysts are well mixed with $LiAlH_4$ after high energy ball-milling, and there exist good contacts between the catalyst and $LiAlH_4$ particles, resulting in the significantly enhanced dehydrogenation kinetics. However, the elemental map of O is much more obvious than that of Fe and Co in these two elemental maps, attributed to oxidation during the specimen preparation process. As a result, deformed and disordered surface regions are produced around them, exhibiting many surface defects, which introduce a larger amount of reaction nucleation sites and hydrogen diffusion channels for the dehydrogenation process. The significant reduction in the crystallite size of nanosized oxide-doped collaborates with the high surface defect density and grain boundaries introduced by the dispersive catalyst properties, improving the desorption properties.

To further analyze the dehydrogenation mechanism of oxide-doped $LiAlH_4$, the activation energy (E_a) of the first two decomposition steps of $LiAlH_4$ with and without catalyst are calculated by using the Kissinger method[47]

$$\frac{d\ln\left(\frac{\beta}{T_p^2}\right)}{d\left(\frac{1}{T_p}\right)} = -\frac{E_a}{R} \quad (2)$$

where β, T_p and R expresses the heating rate, the peak temperature, and the gas constant, respectively. It is noteworthy that DSC measurements are required to be conducted at three different heating rates when utilizing the Kissinger method to calculate E_a. E_a of as-received $LiAlH_4$ for the first two decomposition reactions are 94.8 and 172.3 kJ/mol, respectively,

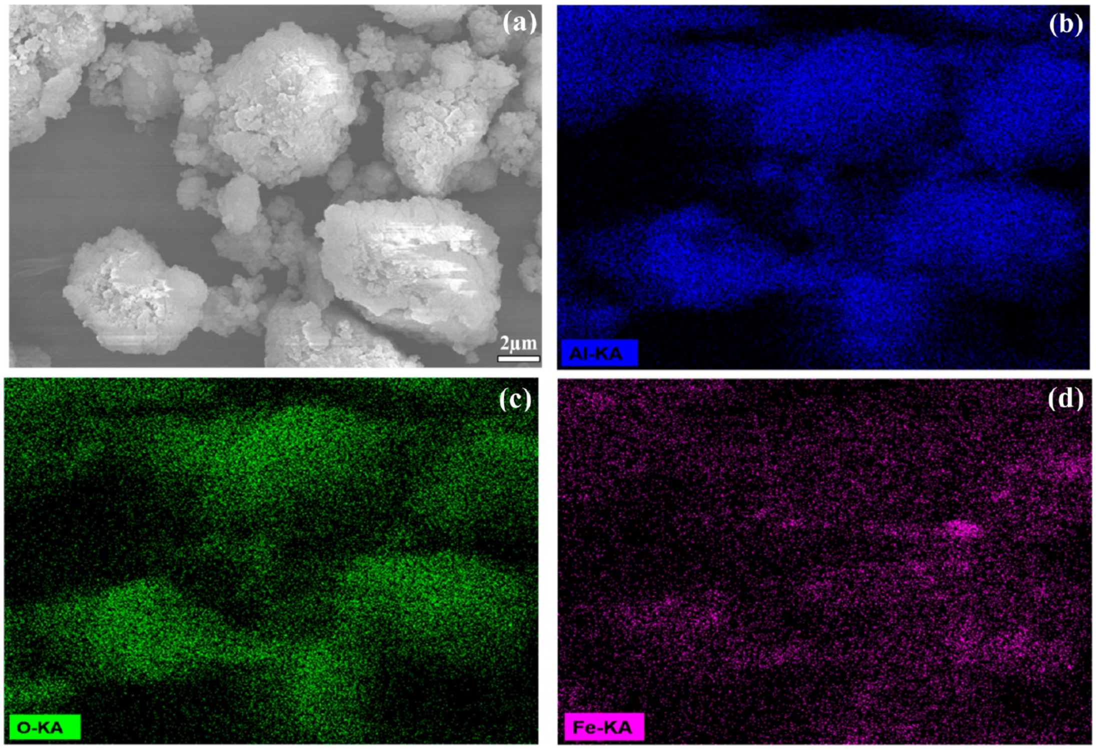

Figure 5. SEM image of (a) $LiAlH_4$ + 5 mol % Fe_2O_3 after ball-milling and elemental maps of (b) aluminum, (c) oxygen, and (d) ferrum.

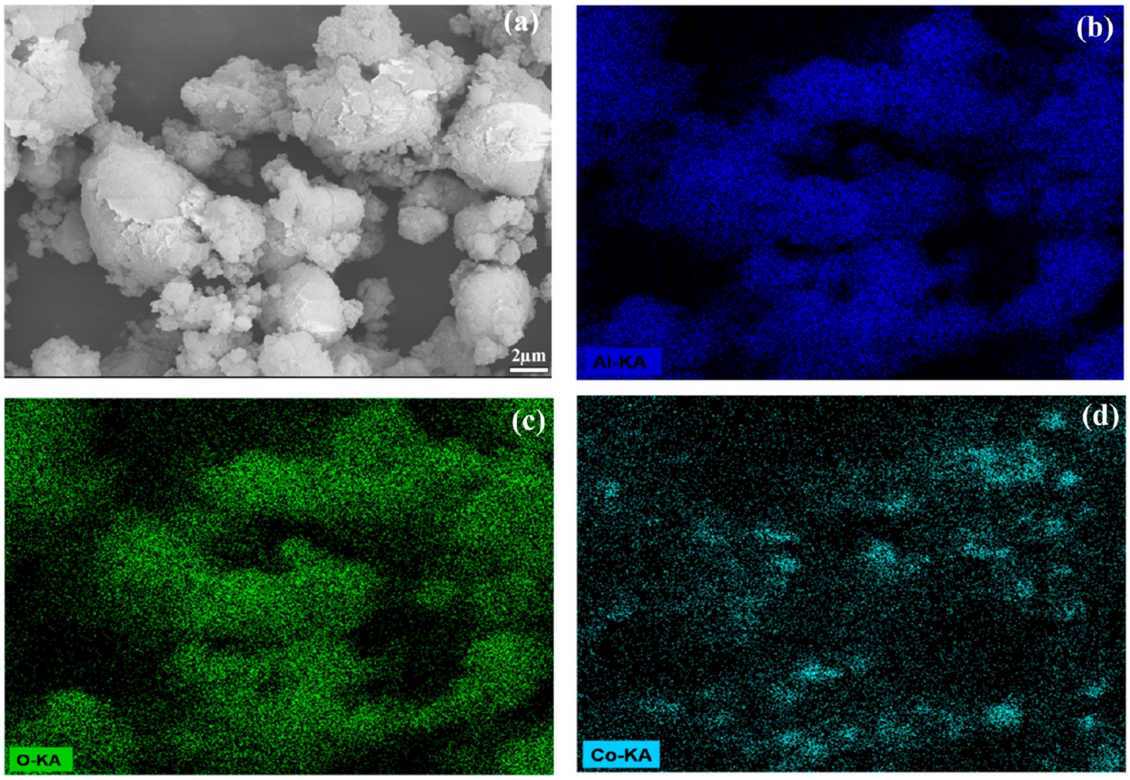

Figure 6. SEM image of (a) $LiAlH_4$ + 5 mol % Co_2O_3 after ball-milling and elemental maps of (b) aluminum, (c) oxygen, and (d) cobalt.

Table 1. Activation Energy of $LiAlH_4$ Doped with Different Catalysts, Calculated by the Kissinger Method

	step 1			step 2			
	E_a (kJ/mol)			E_a (kJ/mol)			
nano catalysts	before doping	after doping	decline rate (%)	before doping	after doping	decline rate (%)	references
TiO_2	114	49	57				13
Nb_2O_5	86	64.5	25	101	79	21.8	3
Fe		60			76.6		48
$MnFe_2O_4$	111.6	66.7	40.2	180.7	75.8	58.1	37
Fe_2O_3	94.8	54.2	42.8	172.3	86.4	50	this work
Co_2O_3	94.8	56	40.9	172.3	92.8	46.1	this work

calculated using eq 2. However, by adding oxide catalysts after ball-milling, E_a of Co_2O_3-doped sample for the first two dehydrogenation steps drastically decreases to 56.0 and 92.8 kJ/mol. Especially for the Fe_2O_3-doped sample, E_a further declines to 54.2 and 86.4 kJ/mol, which is 40.6 and 85.9 kJ/mol lower than that of pristine $LiAlH_4$, respectively. Table 1 shows the comparison of the apparent activation energy (E_a) for various catalysts. The activation energies of the first two dehydrogenation steps for the Co_2O_3 doped sample are 40.9 and 46.1% lower that of pristine $LiAlH_4$. Moreover, E_a decline rate of the Fe_2O_3-doped sample for the first two dehydrogenation steps obtained the maximum of 42.8 and 50.0%, respectively, indicating that the dehydrogenation kinetics of $LiAlH_4$ is evidently improved by the addition of Fe_2O_3 and Co_2O_3 nanopowders. Therefore, the remarkable decrease in E_a for the two decomposition steps further testifies that the dehydrogenation kinetics of $LiAlH_4$ is significantly improved by doping oxide catalysts, while Fe_2O_3 has better catalytic effect.

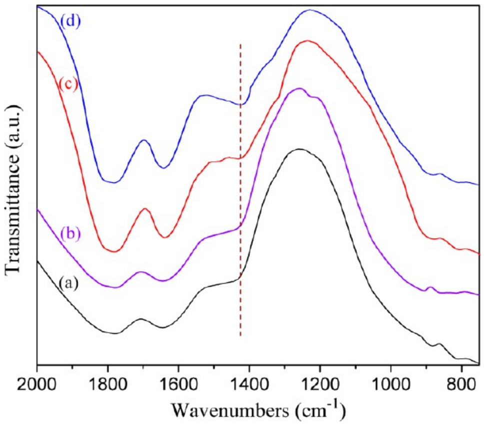

Figure 7. FTIR spectra of (a) as-milled $LiAlH_4$ and (b) 5 mol % Co_2O_3-doped $LiAlH_4$, (c) 5 mol % Fe_2O_3-doped $LiAlH_4$ after ball-milling.

Figure 7 shows the FTIR spectra of (a) as-received $LiAlH_4$, (b) as-milled $LiAlH_4$, (c) 5 mol % Fe_2O_3, and (d) 5 mol % Co_2O_3 doped $LiAlH_4$ after ball-milling in the 750−2000 cm^{-1} wavenumber range. For the as-received $LiAlH_4$ and as-milled $LiAlH_4$, there are two active infrared vibrations of the Al−H bond of $LiAlH_4$ in two regions, (1) Al−H stretching mode ν_3 at 1641

cm^{-1} and (2) Li—Al—H bending mode ν_4 at 885 cm^{-1}. However, an IR absorption peak appears at 1425 cm^{-1} for both doped samples, and it is more notable in the FTIR spectra of the Fe_2O_3-doped sample. On the contrary, no IR absorption peak is visible at the same position in the FTIR spectra of the as-received $LiAlH_4$ and as-milled $LiAlH_4$, as shown in Figure 7. For $LiAlH_4$, there are two regions of active infrared vibrations of the Al—H bonds, (1) Al—H stretching modes between 1600 and 1800 cm^{-1} and (2) Li—Al—H bending modes between 800 and 900 cm^{-1}.[32,49] Meanwhile, for Li_3AlH_6 its active infrared vibration exhibits the Al—H stretching modes between 1500 and 1400 cm^{-1}.[24,49] Through the above analysis, it is reasonable to conclude that the decomposition reaction occurs during the ball-milling process for the oxide-doped $LiAlH_4$ samples, and the decomposition happens more severely by adding Fe_2O_3, which can be validated by the TG and PCT curves.

To identify which reaction happened between $LiAlH_4$, Fe_2O_3, and Co_2O_3 nanoparticles during the ball-milling, the XRD patterns of as-received $LiAlH_4$ and 5 mol % oxides doped composites after ball-milling are shown in Figure 8. For the pattern of as-milled $LiAlH_4$, as shown in Figure 8, except for the diffraction peaks, corresponding to parafilm at 21.4° and 23.8°, no additional peaks can be observed, indicating that the lithium aluminum hydride remains rather highly stabile during high-energy ball-milling treatment.[14] The weak additional peaks of microcrystalline aluminum and Li_3AlH_6 start to appear after ball-milling with Co_2O_3 and Fe_2O_3 nanopowders. Meanwhile, the diffraction peaks of Co_3O_4 are observed at 36.9 and 65.2° for the Co_2O_3-doped sample, suggesting that the temperature in stainless steel milling vial should be higher than 125 °C and deoxidation occurred during the ball-milling process.[6,22,30,42] For the Fe_2O_3-doped sample, the diffraction peaks of $Li_2Fe_{2.4}O_{4.6}$ are observed at 182.0 and 43.2°, demonstrating that the reaction between $LiAlH_4$ and Fe_2O_3 take place during ball-milling by forming a ternary Li—Fe oxide without valence state alteration. At the same time, there is Fe oxide species with a reduced valence state emerging simultaneously. A similar decomposition reaction occurs between $LiAlH_4$ and $MnFe_2O_4$,[37] in which the reaction can take place by forming a ternary Li—Fe oxide and Fe oxide species with a reduced valence state during the ball-milling process.

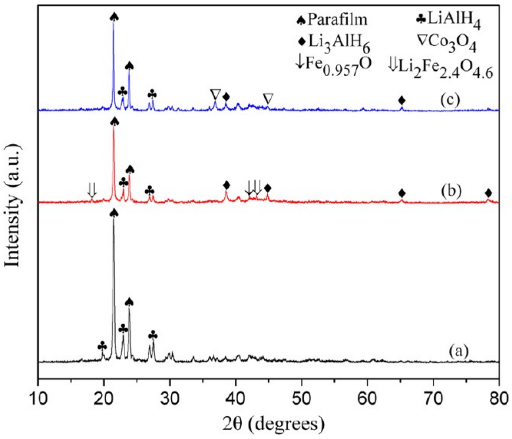

Figure 8. X-ray diffraction spectra of (a) pure $LiAlH_4$, (b) $LiAlH_4$ + 5 mol % Fe_2O_3, and (c) $LiAlH_4$ + 5 mol % Co_2O_3 after ball-milling.

To investigate the change of phase structures of the doped samples during desorption process, XRD scans has been performed on the (a) as-milled $LiAlH_4$, (b) $LiAlH_4$ + 5 mol % Fe_2O_3, (c) $LiAlH_4$ + 5 mol % Co_2O_3 after dehydrogenation at 250 °C, as shown in Figure 9. XRD spectra of the as-milled $LiAlH_4$ after dehydrogenation only consists of Al and LiH as the dehydrogenation products, demonstrating that $LiAlH_4$ and Li_3AlH_6 have completely decomposed after the first two dehydrogenation steps. However, CoO phase is included in the XRD spectra of the Co_2O_3-doped sample when heated up to 250 °C, except for parafilm, Al and LiH phases, suggesting that Co_3O_4 can be further reduced to CoO phase during dehydrogenation process. Further investigation is needed to clarify the role of Co-oxides. By contrast, for the XRD patterns of Fe_2O_3- doped sample there are not only Al and LiH but also $Li_2Fe_{2.4}O_{4.6}$ and $Fe_{0.957}O$ as the dehydrogenation products, which may create surface activation and form a large amount of nucleation sites on the surface of $LiAlH_4$ matrix for dehydrogenation products. Consequently, these dehydrogenated products would possibly contribute to kinetic desorption improvement and provide a synergetic catalytic effect by serving as the active sites for nucleation and growth of the dehydrogenated products, resulting in the shortening of the diffusion distance of the reaction ions.

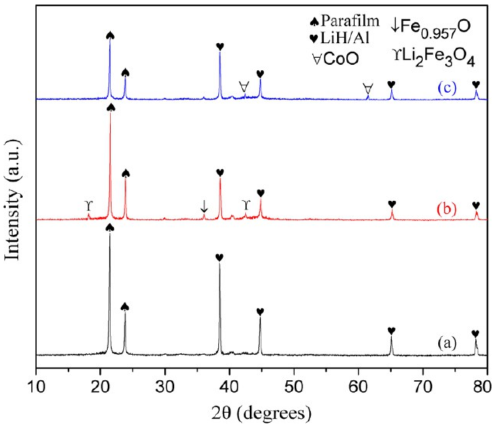

Figure 9. X-ray diffraction spectra of (a) as-milled $LiAlH_4$, (b) $LiAlH_4$ + 5 mol % Fe_2O_3, (c) $LiAlH_4$ + 5 mol % Co_2O_3 after dehydrogenation at 250 °C.

To further analyze the phase composition of dehydrogenated products before and after dehydrogenation, XPS analysis on the Fe_2O_3- and Co_2O_3-doped samples have been performed before and after dehydrogenation, as shown in Figure 10. Figure 10a shows the photoemission spectrum of Fe 2p at 707.0 and 712.0 eV, corresponding to Fe_xO_y[50] and $LiFe_{2.4}O_{4.6}$, respectively. However, for the dehydrogenated Fe_2O_3-doped sample, there exists one Fe 2p peak at 709.6 eV, which corresponds to FeO. Figure 10b shows the Co 2p XPS spectra of $LiAlH_4/Co_2O_3$ sample after ball-milling and dehydrogenation. After ball-milling, only one Co 2p peak is located at 780.0 eV, corresponding to Co_3O_4. Furthermore, for the dehydrogenated sample there are two Co 2p peaks located at 780.0 and 796.5 eV, corresponding to Co_3O_4 and CoO, respectively. However, it should be noted that FeO and Co_3O_4 in the dehydrogenated samples can not be detected in the XRD profiles. These results supplement the XRD results, indicating that Fe and Co species are reduced or transformed during the milling or heating processes. This observation is rather coincidental, since Fe and Co oxides share the same valence of the O anion. Moreover, transition metals always possess good capacity of valence alternation, and they can be reduced to their lower oxidation state by high temperatures in

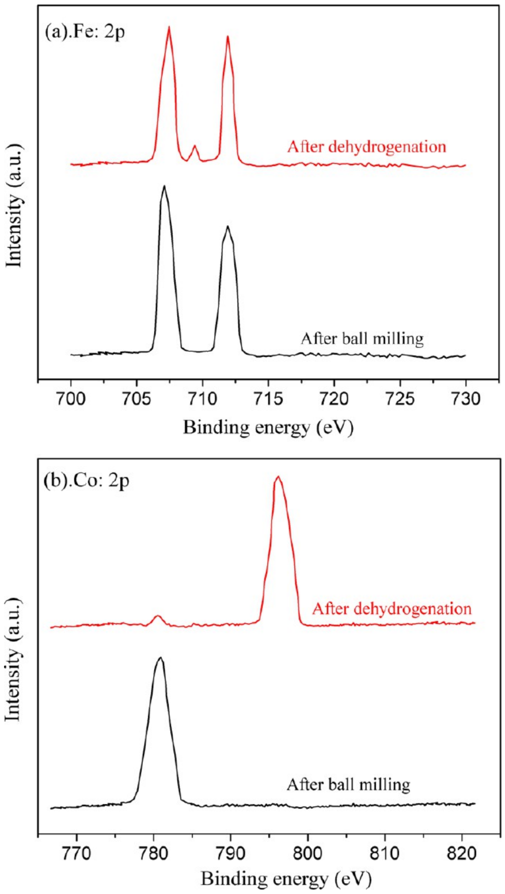

Figure 10. Narrow scan XPS spectra of (a) the Fe_2O_3-doped sample before and after desorption and (b) the Co_2O_3-doped sample before and after desorption.

hydrogen atmosphere. The valence changes of transition metal oxide catalysts during dehydrogenation process are listed in Table 2. By comparing various transition metal oxides, it can be concluded that these multivalence transition metal species may contribute to the improved desorption kinetics.

From the above analyses, the predominant dehydrogenation kinetics, acquired in this work for the doped samples, may be ascribed to the following reasons. First, the significantly reduced particle size and the creation of a large number of defects can introduce a large amount of reaction nucleation sites and hydrogen diffusion channels for the dehydrogenation process. Second, Fe_2O_3 reacts with $LiAlH_4$ during mechanical milling by forming a ternary Li−Fe oxide ($Li_2Fe_{2.4}O_{4.6}$) and Fe oxide ($Fe_{0.957}O$) species, suggesting that trivalent iron oxide can transform into new Fe-containing phases by increasing the high local temperatures during the ball-milling process. After dehydrogenation, the reactions between $LiAlH_4$ and Fe_2O_3 have thoroughly completed, and the Fe species are reduced to their lower oxidation state. Meanwhile, for the Co_2O_3-doped sample the catalysts have been reduced during ball-milling by forming Co oxide species with a reduced valence state, and then further transformed into its lower oxidation state (CoO) when heated to 250 °C after dehydrogenation with a small amount of Co_3O_4, which is hardly detected by XRD. It is believed that these finely dispersed oxygen-deficient Fe and Co oxide nanoparticles could act as catalysts to facilitate the dehydrogenation steps of $LiAlH_4$ by serving as the active sites for nucleation and growth of the dehydrogenated product associated with the shortening of the diffusion paths among the reaction ions. Third, the reduction of Fe_2O_3 and Co_2O_3 during heating can alter the thermodynamics of the reactions by lowering the enthalpy of the dehydrogenation reaction,[3] thus it can also contribute to kinetic desorption improvement, which would be a very attractive topic for further investigation.

4. CONCLUSIONS

In summary, the dehydrogenation properties of $LiAlH_4$ doped with Fe_2O_3 and Co_2O_3 nanoparticles exhibit a dramatic improvement compared with that of as-received $LiAlH_4$. The nonisothermal hydrogen desorption analysis reveals that the addition of increasing amounts of Fe_2O_3 and Co_2O_3 nanoparticles to $LiAlH_4$ results in a progressive reduction of the onset temperature of $LiAlH_4$. The onset temperature of $LiAlH_4$ doped with 7 mol % Fe_2O_3 and Co_2O_3 have reduced by as much as 97 and 93 °C, respectively, compared with the pristine $LiAlH_4$. Between various Fe_2O_3- and Co_2O_3-doped samples, the 5 mol % oxide-doped samples are found to be the optimal materials with the highest released hydrogen capacity and substantially reduced activation energy for the $LiAlH_4$ dehydrogenation. Isothermal volumetric measurements reveal that $LiAlH_4$ + 5 mol % Fe_2O_3 and $LiAlH_4$ + 5 mol % Co_2O_3 samples can release about 7.1 and 6.9 wt % hydrogen in 70 min at 120 °C, whereas the as-received $LiAlH_4$ only releases about 0.3 wt % hydrogen for the same temperature and time. The DSC and Kissinger desorption kinetics analyses reveal that the apparent activation energies of as-received $LiAlH_4$ are 94.8 and 172.3 kJ/mol, while the E_a of the 5 mol % Fe_2O_3-doped sample declines to 54.2 and 86.4 kJ/mol, resulting in declined rates of 42.8 and 50.0%, respectively, for the first two decomposition reactions. Furthermore, FTIR, XRD, and XPS demonstrate that $LiAlH_4$ reacts with Fe_2O_3 during ball-milling by local forming of Fe oxide species with a lower oxidation state and a mixed Li−Fe oxide. These finely dispersed dehydrogenated products would contribute to the dehydrogenation kinetics improvement and provide a synergetic catalytic effect for the remarkably improved dehydrogenation kinetics of

Table 2. The Valence State of Various Transition Metal Oxide Catalysts during the Dehydrogenation Process

		average valence					
transition oxide	transition metal species	initial	after ball-milling	after dehydrogenation	valence change	catalytic performance	reference
$MnFe_2O_4$	Mn	2				superior	37
	Fe	3	4.1	+2.1, +2	Y		
Nb_2O_5	Nb	5	5	+5, +4, +1	Y	superior	3
Cr_2O_3	Cr	3	3	3	N	weak	3
TiO_2	Ti	4	4	4	N	superior	13
Fe_2O_3	Fe	3	+3, +2.09	+2.09, +2.1, +2	Y	superior	this work
Co_2O_3	Co	3	+8/3	+8/3, +2	Y	superior	this work

$LiAlH_4$. On the contrary, nanosized Co_2O_3 particles act as a surface catalyst and are reduced to Co_3O_4 during the ball-milling process, and then translate to CoO when heated to 250 °C. Therefore, it is reasonable to conclude that the finely dispersed Fe oxide, Li−Fe oxide, and Co oxide may contribute to dehydrogenation kinetics improvement and provide a synergetic catalytic effect by serving as active sites for nucleation and growth of the dehydrogenated products, resulting in the shortening of the diffusion distance of the reaction ions. Meanwhile, the reduction of high valence transition metals during heating may play an important role in improving the kinetic desorption of the doped samples. In summary, it is reasonable to conclude that Fe_2O_3 and Co_2O_3 nanoparticles are promising additives for remarkably improving the dehydrogenation performance of $LiAlH_4$, and the Fe_2O_3 nanoadditive is more efficient than the Co_2O_3 nanoadditive.

■ ASSOCIATED CONTENT

Ⓢ Supporting Information

Figure of DSC curves of as-received $LiAlH_4$, $LiAlH_4$ + 5 mol % Fe_2O_3, and $LiAlH_4$ + 5 mol % Co_2O_3 at the heating rates of 6, 9, and 12 °C/min, and figure of the Kissinger plots of as-received $LiAlH_4$, $LiAlH_4$ + 5 mol % Fe_2O_3, and $LiAlH_4$ + 5 mol % Co_2O_3 for the first and second dehydrogenation steps. This material is available free of charge via the Internet at http://pubs.acs.org.

■ AUTHOR INFORMATION

Corresponding Author

*E-mail: ustbliping@126.com. Tel: +86-10-82377286. Fax: +86-10-62334311.

Notes

The authors declare no competing financial interest.

■ ACKNOWLEDGMENTS

The authors thank the National High-Tech R&D Program (863 Program) of China (2006AA05Z132) and China Scholarship Council (CSC) for financial support of this research. A.V. acknowledges support from the National Science Foundation.

■ REFERENCES

(1) Li, L.; Qiu, F. Y.; Wang, Y. J.; Xu, Y. A.; An, C. H.; Liu, G.; Jiao, L. F.; Yuan, H. T. Enhanced Hydrogen Storage Properties of TiN-$LiAlH_4$ Composite. *Int. J. Hydrogen Energy* **2013**, *38*, 3695−3701.

(2) Dathar, G. K.; Mainardi, D. S. Kinetics of Hydrogen Desorption in $NaAlH_4$ and Ti-Containing $NaAlH_4$. *J. Phys. Chem. C* **2010**, *114*, 8026−8031.

(3) Rafi-ud-din, Qu, X. H.; Li, P.; Zhang, L.; Wan, Q.; Iqbal, M. Z.; Rafique, M. Y.; Farooq, M. H. Islam-ud-din. Superior Catalytic Effects of Nb_2O_5, TiO_2, and Cr_2O_3 Nanoparticles in Improving the Hydrogen Sorption Properties of $NaAlH_4$. *J. Phys. Chem. C* **2012**, *116*, 11924−11938.

(4) Michel, K. J.; Ozoliņš, V. Vacancy Diffusion in $NaAlH_4$ and Na_3AlH_6. *J. Phys. Chem. C* **2011**, *115*, 21465−21472.

(5) Ismail, M.; Zhao, Y.; Yu, X. B.; Mao, J. F.; Dou, S. X. The Hydrogen Storage Properties and Reaction Mechanism of the MgH_2-$NaAlH_4$ Composite System. *Int. J. Hydrogen Energy* **2011**, *36*, 9045−9050.

(6) Mao, J. F.; Guo, Z. P.; Leng, H. Y.; Wu, Z.; Guo, Y. H.; Yu, X. B.; Liu, H. K. Reversible Hydrogen Storage in Destabilized $LiAlH_4$-MgH_2-$LiBH_4$ Ternary-Hydride System Doped with TiF_3. *J. Phys. Chem. C* **2010**, *114*, 11643−11649.

(7) Fallas, J. C.; Chien, W. M.; Chandra, D.; Kamisetty, V. K.; Emmons, E. D.; Covington, A. M.; Chellappa, R. S.; Gramsch, S. A.; Hemley, R. J.; Hagemann, H. Raman Spectroscopy Measurements of the Pressure-Temperature Behavior of $LiAlH_4$. *J. Phys. Chem. C* **2010**, *114*, 11991−11997.

(8) Sakaki, K.; Nakamura, Y.; Akiba, E.; Kuba, M. T.; Jensen, C. M. Reversible Vacancy Formation and Recovery during Dehydrogenation-Hydrogenation Cycling of Ti-Doped $NaAlH_4$. *J. Phys. Chem. C* **2010**, *114*, 6869−6873.

(9) Andreasen, A.; Veggea, T.; Pedersena, A. S. Dehydrogenation Kinetics of As-Received and Ball-Milled $LiAlH_4$. *J. Solid State Chem.* **2005**, *178*, 3672−3678.

(10) Vittetoe, A. W.; Niemann, M. U.; Srinivasan, S. S.; McGrath, K.; Kumar, A.; Goswami, D. Y.; Stefanakos, E. K.; Thomas, S. Destabilization of $LiAlH_4$ by Nanocrystalline MgH_2. *Int. J. Hydrogen Energy* **2009**, *34*, 2333−2339.

(11) Resan, M.; Hampton, M. D.; Lomness, J. K.; Slattery, D. K. Effects of Various Catalysts on Hydrogen Release and Uptake Characteristics of $LiAlH_4$. *Int. J. Hydrogen Energy* **2005**, *30*, 1413−1416.

(12) Varin, R. A.; Zbroniec, L. The Effects of Nanometric Nickel (n-Ni) Catalyst on the Dehydrogenation and Rehydrogenation Behavior of Ball Milled Lithium Alanate ($LiAlH_4$). *J. Alloys Compd.* **2010**, *506*, 928−939.

(13) Varin, R. A.; Zbroniec, L.; Czujko, T.; Wronski, Z. S. The Effects of Nanonickel Additive on the Decomposition of Complex Metal Hydride $LiAlH_4$ (lithium Alanate). *Int. J. Hydrogen Energy* **2011**, *36*, 1167−1176.

(14) Balema, V. P.; Pecharsky, V. K.; Dennis, K. W. Solid State Phase Transformations in $LiAlH_4$ during High-Energy Ball-Milling. *J. Alloys Compd.* **2000**, *313*, 69−74.

(15) Zheng, X. P.; Li, P.; An, F. Q.; Wang, G. Q.; Qu, X. H. Effects of Ti and Fe Additives on Hydrogen Release from Lithium Alanate. *Rare Metal Mater. Eng.* **2008**, *37*, 400−403.

(16) Balema, V. P.; Wiench, J. W.; Dennis, K. W.; Pruski, M.; Pecharsky, V. K. Titanium Catalyzed Solid-State Transformations in $LiAlH_4$ during High-Energy Ball-Milling. *J. Alloys Compd.* **2001**, *329*, 108−114.

(17) Chen, J.; Kuriyama, N.; Xu, Q.; Takeshita, H. T.; Sakai, T. Reversible Hydrogen Storage via Titanium-Catalyzed $LiAlH_4$ and Li_3AlH_6. *J. Phys. Chem. B* **2001**, *105*, 11214−11220.

(18) Langmi, H. W.; McGrady, G. S.; Liu, X. F.; Jensen, C. M. Modification of the H_2 Desorption Properties of $LiAlH_4$ through Doping with Ti. *J. Phys. Chem. C* **2010**, *114*, 10666−10669.

(19) Schlapbach, L.; Zuttel, A. Hydrogen-Storage Materials for Mobile Applications. *Nature* **2001**, *414*, 353−358.

(20) Song, Y.; Dai, J. H.; Li, C. G.; Yang, R. Influence of Dopants Ti and Ni on Dehydrogenation Properties of $NaAlH_4$: Electronic Structure Mechanisms. *J. Phys. Chem. C* **2009**, *113*, 10215−10221.

(21) Hima, K. L.; Viswanathan, B.; Srinivasa, M. S. Dehydriding Behaviour of $LiAlH_4$−the Catalytic Role of Carbon Nanofibres. *Int. J. Hydrogen Energy* **2008**, *33*, 366−373.

(22) Rafi-ud-din; Zhang, L.; Li, P.; Qu, X. H. Catalytic Effects of Nano-Sized TiC Additions on the Hydrogen Storage Properties of $LiAlH_4$. *J. Alloys Compd.* **2010**, *508*, 119−128.

(23) Andreasen, A. Effect of Ti-doping on the Dehydrogenation Kinetic Parameters of Lithium Aluminum Hydride. *J. Alloys Compd.* **2006**, *419*, 40−44.

(24) Ares Fernandez, J. R.; Aguey-Zinsou, K. F.; Elsaesser, M.; Ma, X. Z.; Dornheim, M.; Klassen, T.; Bormann, R. Mechanical and Thermal Decomposition of $LiAlH_4$ with Metal Halides. *Int. J. Hydrogen Energy* **2007**, *32*, 1033−1040.

(25) Suttisawat, Y.; Rangsunvigit, P.; Kitiyanana, B.; Muangsinb, N.; Kulprathipanjac, S. Catalytic Effect of Zr and Hf on Hydrogen Desorption/Absorption of $NaAlH_4$ and $LiAlH_4$. *Int. J. Hydrogen Energy* **2007**, *32*, 1277−1285.

(26) Zheng, X. P.; Li, P.; Humail, I. S.; An, F. Q.; Wang, G. Q.; Qu, X. H. Effect of Catalyst $LaCl_3$ on Hydrogen Storage Properties of Lithium Alanate ($LiAlH_4$). *Int. J. Hydrogen Energy* **2007**, *32*, 4957−4960.

(27) Kojima, Y.; Kawai, Y.; Matsumoto, M.; Haga, T. Hydrogen Release of Catalyzed Lithium Aluminum Hydride by a Mechanochemical Reaction. *J. Alloys Compd.* **2008**, *462*, 275−278.

(28) Sun, T.; Huang, C. K.; Wang, H.; Sun, L. X.; Zhu, M. The Effect of Doping $NiCl_2$ on the Dehydrogenation Properties of $LiAlH_4$. *Int. J. Hydrogen Energy* **2008**, *33*, 6216−6221.

(29) Liu, S. S.; Sun, L. X.; Zhang, Y.; Xu, F.; Zhang, J.; Chu, H. L.; Fan, M. Q.; Zhang, T.; Song, X. Y.; Grolier, J. P. Effect of Ball Milling Time on the Hydrogen Storage Properties of TiF_3-Doped $LiAlH_4$. *Int. J. Hydrogen Energy* **2009**, *34*, 8079−8085.

(30) Ismail, M.; Zhao, Y.; Yu, X. B.; Dou, S. X. Effects of NbF_5 Addition on the Hydrogen Storage Properties of $LiAlH_4$. *Int. J. Hydrogen Energy* **2010**, *35*, 2361−2367.

(31) Varin, R. A.; Zbroniec, L. Fast and Slow Dehydrogenation of Ball Milled Lithium Alanate ($LiAlH_4$) Catalyzed with Manganese Chloride ($MnCl_2$) as Compared to Nanometric Nickel Catalyst. *J. Alloys Compd.* **2011**, *509S*, S736−S739.

(32) Li, Z. B.; Liu, S. S.; Si, X. L.; Zhang, J.; Jiao, C. L.; Wang, S.; Liu, S.; Zou, Y. J.; Sun, L. X.; Xu, F. Significantly Improved Dehydrogenation of $LiAlH_4$ Destabilized by K_2TiF_6. *Int. J. Hydrogen Energy* **2012**, *37*, 3261−3267.

(33) Fu, J.; Röntzsch, L.; Schmidt, T.; Tegel, M.; Weißgärber, T.; Kieback, B. Comparative Study on the Dehydrogenation Pproperties of $TiCl_4$-Doped $LiAlH_4$ Using Different Doping Techniques. *Int. J. Hydrogen Energy* **2012**, *37*, 13387−13392.

(34) Zheng, X. P.; Zheng, J. J.; Ma, Q. H.; Liu, S. L.; Feng, X.; Lin, X. B.; Xiao, G. Study on Dehydrogenation Properties of the $LiAlH_4$-NH_4Cl System. *J. Alloys Compd.* **2013**, *551*, 508−511.

(35) Ismail, M.; Zhao, Y.; Yu, X. B.; Nevirkovets, I. P.; Dou, S. X. Significantly Improved Dehydrogenation of $LiAlH_4$ Catalysed with TiO_2 Nanopowder. *Int. J. Hydrogen Energy* **2011**, *36*, 8327−8334.

(36) Rafi-ud-din; Qu, X. H.; Li, P.; Zhang, L.; Ahmad, M. Hydrogen Sorption Improvement of $LiAlH_4$ Catalyzed by Nb_2O_5 and Cr_2O_3 Nanoparticles. *J. Phys. Chem. C* **2011**, *115*, 13088−13099.

(37) Zhai, F. Q.; Li, P.; Sun, A. Z.; Wu, S.; Wan, Q.; Zhang, W. N.; Li, Y. L.; Cui, L. Q.; Qu, X. H. Significantly Improved Dehydrogenation of $LiAlH_4$ Destabilized by $MnFe_2O_4$ Nanoparticles. *J. Phys. Chem. C* **2012**, *116*, 11939−11945.

(38) Liu, S. S.; Li, Z. B.; Jiao, C. L.; Si, X. L.; Yang, L. N.; Zhang, J.; Zhou, H. Y.; Huang, F. L.; Gabelica, Z.; Schick, C.; et al. Improved Reversible Hydrogen Storage of $LiAlH_4$ by Nano-Sized TiH_2. *Int. J. Hydrogen Energy* **2013**, *38*, 2770−2777.

(39) Zheng, X. P.; Liu, S. L. Study on Hydrogen Storage Properties of $LiAlH_4$. *J. Alloys Compd.* **2009**, *481*, 761−763.

(40) Ismail, M.; Zhao, Y.; Yu, X. B.; Ranjbar, A.; Dou, S. X. Improved Hydrogen Desorption in Lithium Alanate by Addition of SWCNT-Metallic Catalyst Composite. *Int. J. Hydrogen Energy* **2011**, *36*, 3593−3599.

(41) Zhang, H.; Cao, Z.; Sun, L. X.; Sun, Y. J.; Xu, F.; Liu, H.; Zhang, J.; Huang, Z. Q.; Jiang, X.; Li, Z. B.; et al. Improved Dehydrogenation/Rehydrogenation Performance of $LiBH_4$ by Doping Mesoporous Fe_2O_3 or/and TiF_3. *J. Therm. Anal. Calorim* **2013**, *112*, 1407−1414.

(42) Pataha, A.; Takasaki, A.; Szmyd, J. S. Influence of Multiple Oxide (Cr_2O_3/Nb_2O_5) Addition on the Sorption Kinetics of MgH_2. *Int. J. Hydrogen Energy* **2009**, *34*, 3032−3037.

(43) Yuan, H. P.; Zhang, X. G.; Li, Z. N.; Ye, J. H.; Guo, X. M.; Wang, S. M.; Liu, X. P.; Jiang, L. J. Influence of Metal Oxide on $LiBH_4$/$2LiNH_2$/MgH_2 System for Hydrogen Storage Properties. *Int. J. Hydrogen Energy* **2012**, *37*, 3292−3297.

(44) Mashkoor, A.; Rafi-ud-Din; Cao, F. P.; Jing, Z. Investigation of Hydrogen Storage Capabilities of ZnO-Based Nanostructures. *J. Phys. Chem. C* **2010**, *114*, 2560−2565.

(45) Zheng, X. P.; Li, P.; Qu, X. H. Effect of Additives on the Reversibility of Lithium Alanate ($LiAlH_4$). *Rare Metal Mat. Eng.* **2009**, *38*, 766−769.

(46) McCarty, M.; Maycock, J. N.; Verneker, V. R. P. Thermal Decomposition of Lithium Aluminum Hydride. *J. Phys. Chem.* **1968**, *72*, 4009−4014.

(47) Kissinger, H. E. Reaction Kinetics in Differential Thermal Analysis. *Anal. Chem.* **1957**, *29*, 1702−1706.

(48) Varin, R. A.; Parviz, R. The Effects of the Micrometric and Nanometric Iron (Fe) Additives on the Mechanical and Thermal Dehydrogenation of Lithium Alanate ($LiAlH_4$), its Self-Discharge at Low Temperatures and Rehydrogenation. *Int. J. Hydrogen Energy* **2012**, *37*, 9088−9102.

(49) Liu, S. S.; Zhang, Y.; Sun, L. X.; Zhang, J.; Zhao, J. N.; Xu, F.; Huang, F. L. The Dehydrogenation Performance and Reaction Mechanisms of Li_3AlH_6 with TiF_3 Additive. *Int. J. Hydrogen Energy* **2010**, *35*, 4554−4561.

(50) Li, P.; Wan, Q.; Li, Z. L.; Zhai, F. Q.; Li, Y. L.; Cui, L. Q.; Qu, X. H.; Volinsky, A. A. MgH_2 Dehydrogenation Properties Improved by $MnFe_2O_4$ Nanoparticles. *J. Power Sources* **2013**, *239*, 201−206.